A comprehensive analysis of wing rock dynamics for slender delta wing configurations

A comprehensive analysis of wing rock dynamics for slender delta wing configurations

Giorgio Guglieri

Abstract The paper deals with the study of an analytical model of wing rock, based on parameter identification of experimental data. The experiments were performed in the Aeronautical Laboratory of Politecnico di Torino, in the D3M Low Speed Wind Tunnel, on a 80° delta wing with a modular fuselage, designed with a cylindrical forebody and a conical nose tip. Free-to-roll tests have been used to determine build up and limit cycle characteristics of wing rock. An analytical nonlinear model was derived. Parameters were identified by means of least squares approximation of experimental data with coherent initial conditions. The consistency of time histories, reproduced by numerical integration, was also analyzed. This formulation correctly predicts stable limit cycles for a wide range of airspeeds, angles of attack, and release roll angles. Finally, the impact of aircraft configuration on wing rock parameters is here outlined.

Keywords Aircraft dynamics · Delta wing aerodynamics · Vortex dynamics

Nomenclature

a_i nondimensional coefficients
b wing span
c wing root chord
C_l rolling moment coefficient (L/qSb)
$C_{l_{\text{aer}}}$ rolling moment coefficient (aerodynamic term)
C_{l_f} rolling moment coefficient (friction term)
f oscillation frequency
I_{xx} model inertia
k reduced oscillation frequency ($\pi f b/V$)
ℓ oscillation cycle
L rolling moment
q dynamic pressure ($\rho V^2/2$)
S model wing surface
S_{wt} wind tunnel cross section
Re Reynolds number (based on c)
t time
$\hat{t}$ nondimensional time (t/t^*)
t^* reference time ($b/2V$)
TPI Politecnico di Torino
V airspeed
WR Wing Rock
α angle of attack
β angle of sideslip
μ_f rolling moment coefficient (friction rate coefficient)
φ roll angle
φ_0 release roll angle
$\Delta\varphi$ oscillation amplitude in roll
Λ sweep angle
ρ air density
$\cdot$ time derivative

1 Introduction

Wing rock is a self-sustained large-amplitude oscillation in roll that may exhibit a dynamically stable limit cycle. The final state is generally stable and characterized by both large roll attitudes and coupling with directional modes. This phenomenon can seriously limit the operational effectiveness of aircraft utilizing highly swept wings during take-off, landing, and maneuvering flight.

The motion has been observed in flight, but has been difficult to explain because of its similarity to a lightly damped Dutch-roll mode. The evidence suggests that the wing rock motion is a limit cycle oscillation wherein the amplitude and period of the motion is solely a result of aerodynamic non-linearities. This is a contrast to the response of a lightly damped Dutch-roll mode where the amplitude is determined by the initial conditions. The presence of mechanical hysteresis in stability augmentation systems can also give rise to limit cycle motions, and this situation should not be confused with either the Dutch-roll or aerodynamic hysteresis.

The main aerodynamic parameters of wing rock are: (i) angle of attack, (ii) angle of sweep, (iii) leading edge extensions, and (iv) slender forebody. Therefore, the aircraft that are susceptible to the wing rock phenomenon are those containing these parameters, such as aircraft with highly swept wings operating with leading edge extensions. Such aircraft include many modern combat aircraft such as Panavia Tornado, Eurofighter Typhoon, F-16, F-18, and the supersonic civil transport aircraft Concorde as examples.

The onset of wing rock is related with a nonlinear variation of roll damping derivative with α, sideslip angle β, oscillation frequency and amplitude [1].

Wing rock is primarily observed by means of wind tunnel free-to-roll experiments for very slender delta wings (leading edge sweep $\Lambda \geq 75°$) at high angles of attack ($\alpha \geq 25°$). For these experimental conditions, unstable roll damping is found for moderate bank angles φ (i.e., moderate sideslip). Differently, dynamic roll stability occurs for larger roll displacements φ (i.e., larger sideslip). The combined effect of dihedral static stability (i.e., the restoring moment) and nonlinear roll damping is the basic explanation for the presence of the limit cycle.

Aircraft configurations with slender forebodies are affected by wing rock, due to the unsteady interaction between primary forebody vortices and lifting surfaces (leading edge extensions, wing, and stabilizers). Therefore, the oscillatory dynamics is substantially irregular in terms of amplitude and frequency.

The forebody flow pattern (see [5] for a very complete discussion of the subject) is mainly characterized by a primary pair of vortices (in bound secondary vortical systems play a marginal role) emanating from the apex and separating from the body along the leeward side of the fore part of the fuselage. Typically, the vortex pair (if the fuselage body is slender) becomes asymmetric for angles of attack exceeding the magnitude of the apex angle, measured as the angle enclosed by the tangents to the ogive nose shape (usually above 30°). This asymmetry is present for symmetric flight conditions and the direction of prevalent sideforce is determined by ogive surface microasymmetries (roughness). The vortex cores (longitudinal axis of the vortices) are displaced apart from the fuselage and, if the flow is asymmetric, they induce an unbalanced interference with the lifting surfaces downstream (leading edge extensions, wing, and empennages). These changes in the flow topology affect the behavior of the wing and are also believed to give rise to critical states [4]. A critical state is defined as the value of the motion variable (e.g., the angle of attack or roll angle) where there is a discontinuity in the aerodynamic coefficient or its derivative.

The forebody-induced wing rock may be suppressed either by changing forebody cross-section and slenderness or by the adoption of forebody vortex control techniques (boundary layer suction-blowing or movable forebody strakes) [2]. Forebody strakes are usually installed close to the ogive apex, either fixed or deployable. The strakes induce the separation of the flow and the formation of the vortices is fixed along the leading edge of these nonlifting surfaces. Furthermore, if deployed symmetrically, they induce a symmetric behavior of the forebody vortices, canceling out the destabilizing sideforce component. If deployed asymmetrically, they enhance the asymmetry and can be used as an auxiliary control, for high angle of attack directional steering. In any case, due to their negligible lifting contribution, they do not change the lift of the overall configuration, as extensively demonstrated in [3].

Indeed, the aerodynamic regime on these configurations is dominated by vortical flows [5]. Evidence is given that, during wing rock oscillations, the normal

position in the crossflow plane of vortex cores is affected by hysteresis. The roll angular velocity greatly influences both the pressure distribution on the wing surface and the roll damping. Furthermore, the vortex strength varies during the wing rock process. Free-to-roll and forced oscillation tests on slender delta wings indicated that wing rock build up is substantially promoted by roll damping decrease at high angles of attack.

The systematic approach to the study of wing rock is based on wind tunnel experimental investigation of roll dynamics [6–13] for highly swept delta wing models (see [12, 13] for an interfacility comparison). These experiments were performed in nonuniform test conditions (i.e., accuracy of the data acquisition system, model size, equivalent dihedral, roll inertia, size of the test section, geometry of the support, type of bearings, and levels of friction). As a matter of fact, especially Arena [8–10] conducted a very thorough experimental study of the wing rock motion on a flat plate delta wing. This study provides an interesting example of the importance of unsteady aerodynamics on the wing rock motion. What makes the study unique is the measurement of the unsteady aerodynamics, surface pressures, and off-surface location of the leading-edge vortices in combination with a numerical simulation of the wing rock motion. Because of the completeness of this study, it was used as a reference for the present experimental program. The geometries of different reference models and the blockage factors S/S_{wt} are presented in Table 1. Wind tunnel tests are performed with one degree of freedom free-to-roll rigs, neglecting the typical couplings observed in real aircraft motion dynamics. These simplified geometries exhibit stable limit cycles and correctly reproduce the dominant effect of primary wing vortices. Differently, the analysis of complete aircraft roll dynamics is quite difficult, as the relevant aerodynamic interactions between forebody, lifting surfaces, and empennages may alter the onset mechanism of wing rock.

Diverse mathematical formulations of the differential equation governing the single degree of freedom approximation of the roll mode were suggested and validated by means of a complete parametric identification using both numerical simulations and experimental data:

$$C_l(t) = a_0 + a_1\varphi + a_2\dot{\varphi} + a_3|\varphi|\dot{\varphi} + a_4|\dot{\varphi}|\dot{\varphi}$$
(Ref. [1])

Table 1 The geometrical characteristics of several 80° delta wing models

Model	c [mm]	b [mm]	S/S_{wt}
Ref. [6]	428	150	0.032
Ref. [7]	1760	620	0.041
Ref. [8]	422	149	0.085
Ref. [11]	200	70	0.019
Refs. [12, 13]	479	169	0.006

$$C_l(t) = a_0(\varphi) + a_1(\varphi)\dot{\varphi} + a_2(\varphi)\dot{\varphi}^2 + a_3(\varphi)\dot{\varphi}^3 + a_4(\varphi)\dot{\varphi}^4 \quad \text{(Ref. [11])}$$

$$C_l(t) = a_1\varphi + a_2\dot{\varphi} + a_3\varphi^3 + a_4\varphi^2\dot{\varphi} + a_5\varphi\dot{\varphi}^2$$
(Ref. [14])

$$C_l(t) = a_0\varphi + a_1\dot{\varphi} + a_2|\dot{\varphi}|\dot{\varphi} + a_3\varphi^3 + a_4\varphi^2\dot{\varphi}$$
(Refs. [12, 13])

Accurate modeling of wing rock is essential to design control systems able to suppress or alleviate this form of degraded stability. This paper tries to contribute to this field, providing a comprehensive parametric model for wing rock dynamics of a 80° delta wing configuration, with and without slender forebody.

2 Parametric model

The considered analytical model was derived and experimentally validated in [12, 13]. The nonlinear differential equation (single degree of freedom roll dynamics) which describes the free motion of the roll angle φ is

$$\ddot{\varphi} + a_0\varphi + a_1\dot{\varphi} + a_2|\dot{\varphi}|\dot{\varphi} + a_3\varphi^3 + a_4\varphi^2\dot{\varphi} = \ddot{\varphi} - \hat{C}_l(\varphi) = 0 \tag{1}$$

where a_0, a_1, a_2, a_3, a_4 are the parameters relative to the experimental conditions (i.e., angle of attack, Reynolds number, and wing characteristics). The time derivatives are nondimensional (the time scaling factor is $b/2V$).

Note that

$$\hat{C}_l(\varphi) = \frac{qSb}{I_{xx}} \cdot C_l(\varphi) \tag{2}$$

is the normalized rolling moment coefficient, i.e., the external driving torque.

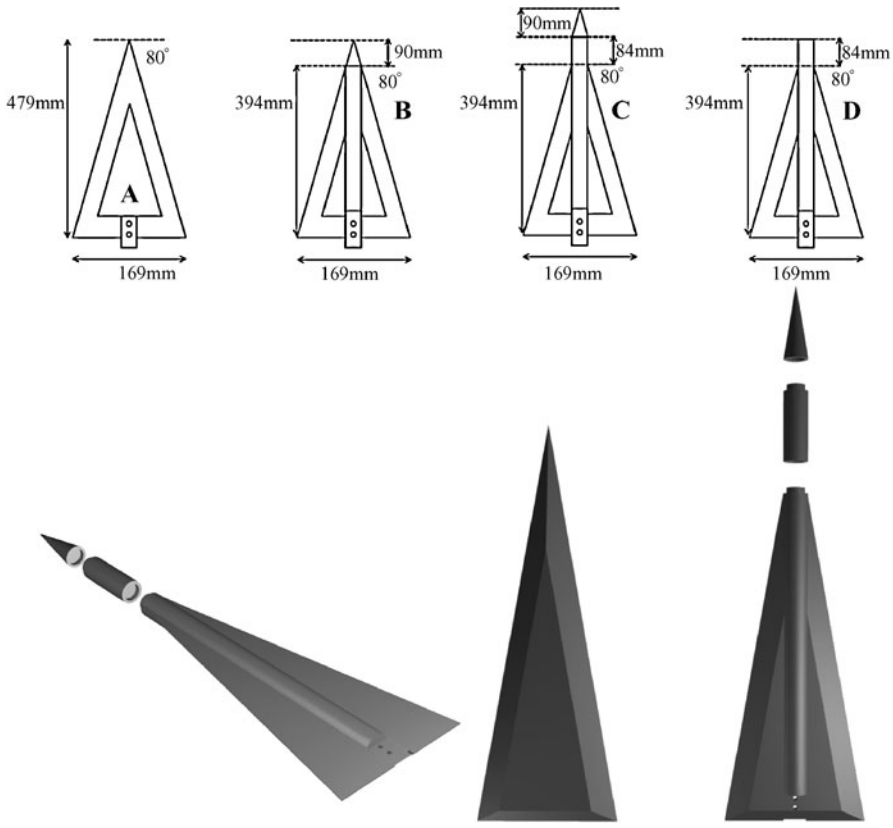

Fig. 1 The 80° delta wing model configurations: model A (wing), model B (wing + nose tip), model C (wing + forebody + nose tip), model D (wing + forebody)

The restoring moment $a_0\varphi + a_3\varphi^3$ exhibits a typical trend with softening of linear stiffness a_0 (Duffing equation). As a consequence the system is statically divergent for $\varphi > \sqrt{-a_0/a_3}$. The damping coefficient $(a_1 + a_4\varphi^2)$ is nonlinear and negative for $\varphi < \sqrt{-a_1/a_4}$ (Van der Pol equation). The system is dynamically unstable for lower roll angles becoming stable as φ increases up to the inversion point. The coordinate for this dynamic stability cross-over is not coincident with limit cycle amplitude, as the stability of final state occurs when

$$E \equiv \oint_{\ell} \hat{C}_l(\varphi)\, d\varphi = 0 \tag{3}$$

This condition is required for the balance between dissipation and generation of energy E and for a stable oscillatory limit cycle. Dynamic stability and limit cycle characteristics are also influenced by the additional damping produced by the term $a_2|\dot{\varphi}|\dot{\varphi}$. The equivalence of reduced order models with the experimental system is discussed in detail in [12, 13].

3 Experimental activity

Free-to-roll experiments were performed on a set of delta wing models (see Fig. 1).

The first set of experiments was performed on model A for $\alpha = 21°$–$45°$, $V = 15$ m/s–40 m/s, Re = 486000–1290000, and $\varphi_0 = 0°$–$90°$ ($\dot{\varphi}_0 = 0$). These results were presented in [12, 13]. Additional experimental data were obtained on the complete set of models A, B, C, and D for $\alpha = 25°$–$45°$, $V = 30$ m/s, Re = 950000 and $\varphi_0 = 20°$ ($\dot{\varphi}_0 = 0$). A special set of measurement was performed on model C for $\alpha = 27.5°$ and $\alpha = 32.5°$ with variable airspeed $V = 15$–40 m/s and $\varphi_0 = \pm 90°$ ($\dot{\varphi}_0 = 0$). These last results are discussed in the present paper.

The experimental tests were carried out in the D3M low speed wind tunnel at Politecnico di Torino. The test section is circular (3 m in diameter). The turbulence level is 0.3 % at $V = 50$ m/s.

The model was a 80° delta wing with sharp leading and trailing edges, made in aluminum alloy. Sharp leading edge delta wings aerodynamics exhibit a minimal sensitivity to the effects of Reynolds number as

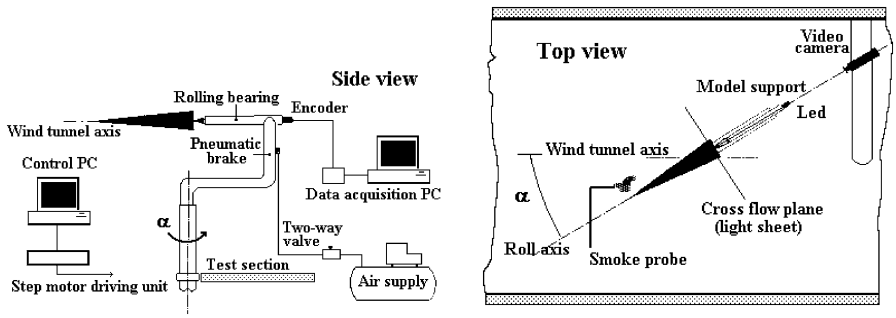

Fig. 2 The experimental setup

the separation of wing primary vortices is fixed along the leading edge. The results presented in [12, 13] confirm this insensitivity for model A. The dimensions are: root chord $c = 479$ mm, span $b = 169$ mm, thickness 12 mm, and bevel angle 20°. Four different model configurations were obtained by adding a cylindrical forebody (length 84 mm) and a conical nose tip (length 90 mm), as explained in Fig. 1. The overall length of the complete model with fuselage and nose tip (model C) is a 568 mm. A set of experiments was performed with a modified version of model C with two symmetrical forebody strakes (installed with −30° negative dihedral). The wing longitudinal body axis and the bearings axis coincide. The rotating system was statically balanced. Note that feature is not verified in some of the previous experiments available for reference.

The C-shaped support (Fig. 2) was mounted on a vertical strut which was able to rotate so that the angle of attack could change while the model centroid remained at the center of the test section.

The model was connected to a horizontal shaft supported by rolling bearings. In order to minimize the friction of the angular transducer, the motion of the wing was measured by an optical encoder, linked with the rotating shaft using an elastic joint without backlash. This digital transducer was able to provide a resolution of 0.45°/bit.

A pneumatic brake was adopted to keep the wing in the initial angular position. During wind on runs, a trigger signal was sent by the operator to the data acquisition unit and the model was released by a pneumatic cylinder fit inside of the vertical arm of the C-shaped support.

The digital signals generated by the encoder, which identify the sign, the increment and the zero crossing of $\varphi(t)$, were conditioned by an electronic device consisting of an incremental counter and a 12 bit digital to analog converter. Both the analog output and the zero crossing trigger signal were multiplexed with a rate of 50 samples/s over a period of 45 s. The data acquisition system was based on a 12 bit analog to digital converter and an oscilloscope for the real time signal monitoring.

The amplitude and the oscillation frequency of the limit cycles were identified after the numerical elaboration of the time histories $\varphi(t)$ with a spectral analyzer. The angular rates were evaluated numerically.

The rolling moment coefficient was evaluated considering that

$$C_l = \frac{I_{xx}}{qSb}\ddot{\varphi} \tag{4}$$

where $I_{xx} = 0.0008738$ Kg m^2 is the moment of inertia about the roll axis for model A and $I_{xx} = 0.0008896$ Kg m^2 for model C.

The coefficient C_l includes the effect of friction (C_{l_f}):

$$C_l = C_{l_{\text{aer}}} + C_{l_f} = C_{l_{\text{aer}}} + C_{l_{0_f}} + \mu_f \dot{\varphi} \tag{5}$$

where $C_{l_{\text{aer}}}$ is the aerodynamic rolling moment coefficient. Friction was neglected taking into account that the limit cycle parameters $(\Delta\varphi, k)$ for model A measured at TPI are very similar to those presented in [8] for comparable test conditions (see Fig. 3). The experimental setup adopted by Arena and Nelson is definitely frictionless as the rotating shaft is supported by air bearings. Therefore, these data are taken as a reference to estimate the impact of friction on TPI measurements. The trend of reduced frequency is coincident but shifted to higher values. This difference is a direct consequence of the different rotational inertia of the experimental apparatus adopted in [8]. The experiments performed by Arena and Nelson establish that the oscillation frequency is proportional to $1/\sqrt{I_{xx}}$ and that the amplitude $\Delta\varphi$ is not substantially

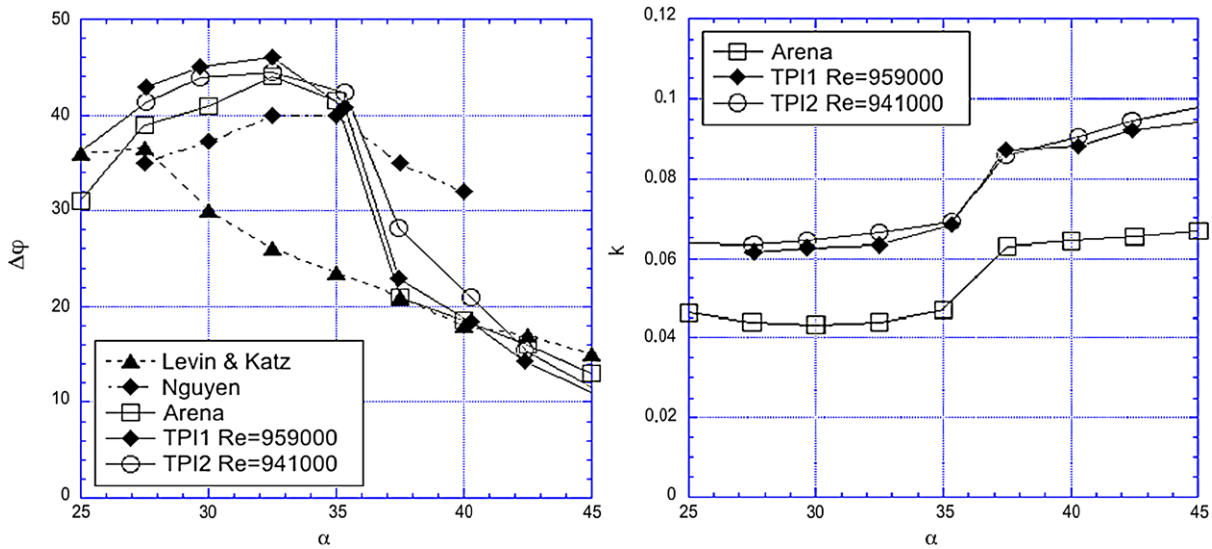

Fig. 3 The experimental limit cycle characteristics ($\Delta\varphi$ is the oscillation amplitude in roll and $k = \pi f b / V$ is the reduced oscillation frequency) for several 80° delta wing models at different angles of attack α

changed by I_{xx}. Anyway, the inertial scaling of the results performs correctly with a perfect overlap, as confirmed by the comparison presented in [12, 13]. As a further comment, the tests performed by Hanff in [15] on a free-to-roll apparatus similar to the TPI rig demonstrate that only the constant friction term $C_{l_{0_f}}$ is required to model the system friction (if required), regardless of the angular velocity and loads acting on the wing. A direct measurement of the breakout torque due to friction in wind off conditions confirmed that this term is very small for the TPI oscillatory rig ($L = 4.5 \cdot 10^{-4}$ Nm equivalent to 0.1 % of the averaged aerodynamic term for $V = 30$ m/s). It must also be observed that the wing oscillations were always immediately triggered as the pneumatic brake fit into the TPI support system was released (at least for model A), even for $\varphi_0 \approx 0$. A very interesting analysis of the effects of model axis of rotation and friction due to bearings on wing rock experimental data is also given in [16].

In [17, 18], an extensive derivation of criteria for inertia similitude between different models, or model and aircraft, is given. These criteria state that similitude is ensured when the two configurations possess the same nondimensional ratio $I_{xx}/\rho b^5$. The nondimensional inertias for different models and aircraft are compared in [12, 13]. This analysis demonstrates that relevant scaling factors are required in order to compare in-flight wing rock with free-to-roll experiments. Similar factors apply for models with the same geometry tested in different wind tunnels.

4 Results

The wing rock phenomenon (see Fig. 4) becomes stable after a build up phase. These oscillations are sustained around a state at which the energy generation at lower amplitudes and the dissipation at larger amplitudes are balanced. The build up phase for model A (basic winged model configuration for $\alpha = 30°$) is characterized by a very rapid increase of oscillation amplitude with fast convergence to limit cycle. Differently, the build up phase for model C (complete wing-body configuration) is very progressive with a longer transient. After that intermediate phase, the final state is finally reached. The plot of the experimental results shows that the center of the elliptic cycles is shifted from the origin ($\Delta\varphi \leq 2.5°$). This asymmetry is a consequence of the support interference. Static flow visualizations on model A [12, 13] confirmed that the wing vortices were slightly displaced even for $\varphi = 0°$.

The effect of model configuration on the final state parameters (amplitude and reduced frequency) for increasing angles of attack is presented in Fig. 5. The presence of the fuselage induces a reduction of oscillation amplitudes as if (at least apparently) the aerodynamic damping of the system was increased with

respect to the wing only configuration (model A). All configurations exhibit an increase of amplitudes $\Delta\varphi$ followed by a sharp reduction for larger angles of attack, due to the presence of vortex breakdown on the wing (stabilizing effect canceling the hysteresis on vortex displacements that drives wing rock dynamics). Stable limit cycles are still observed up to $\alpha = 45°$ (model A). Differently, the oscillations are completely suppressed for $\alpha \geq 45°$ for the other models equipped with fuselage. Another interesting feature is the scaled similarity for the trend of amplitudes of models A and B (wing-body configuration with nose cone only). This point suggests that the presence of the cone apex alters the damping (scaled limit cycle amplitudes) while the presence of the forebody is a dominant factor with a major nonlinear effect for the characteristics of limit cycle (models C and D), generated by the asymmetric behavior of forebody vortices. As a matter of fact, the vortices generated on the apex of the fuselage for model B are immediately interacting with the primary wing vortices without developing asymmetric α-dependent patterns, typical of slender forebodies (models C and D). Model C shows an interesting singularity for $\alpha = 27.5°$ as wing rock oscillations are not triggered (see Fig. 14). The trend of oscillation amplitudes for model D shows that the suppression of wing rock at higher angles of attack is anticipated: the wake disturbances generated by the blunt fuselage apex promote—through their interference—the breakdown of wing vortices (stabilizing effect). The presence of the fuselage also scales down the limit cycle reduced frequencies. This is a consequence of the alteration of aerodynamic damping brought into the system by the additional forebody vortex dynamics superimposed to wing vortices. The onset of breakdown for wing vortices triggers a sharp frequency increase for

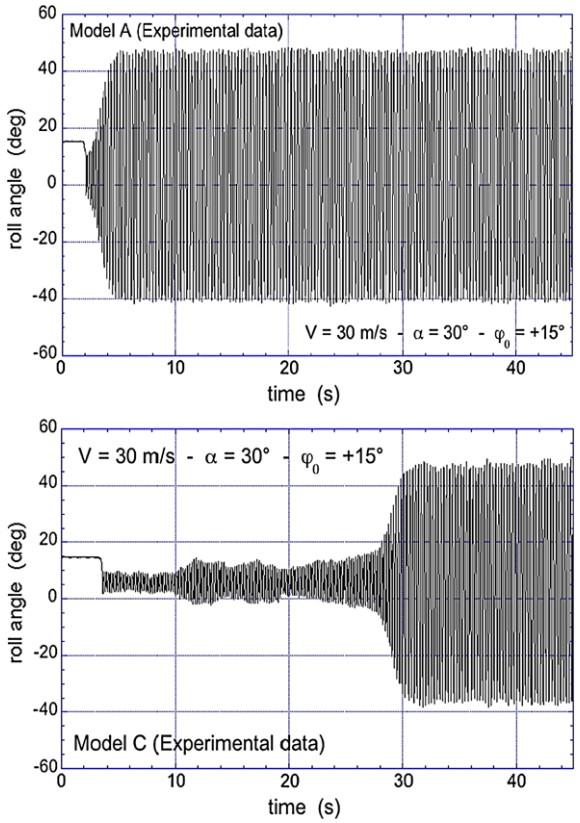

Fig. 4 Wing rock oscillatory dynamics: build up and limit cycle (models A and C)

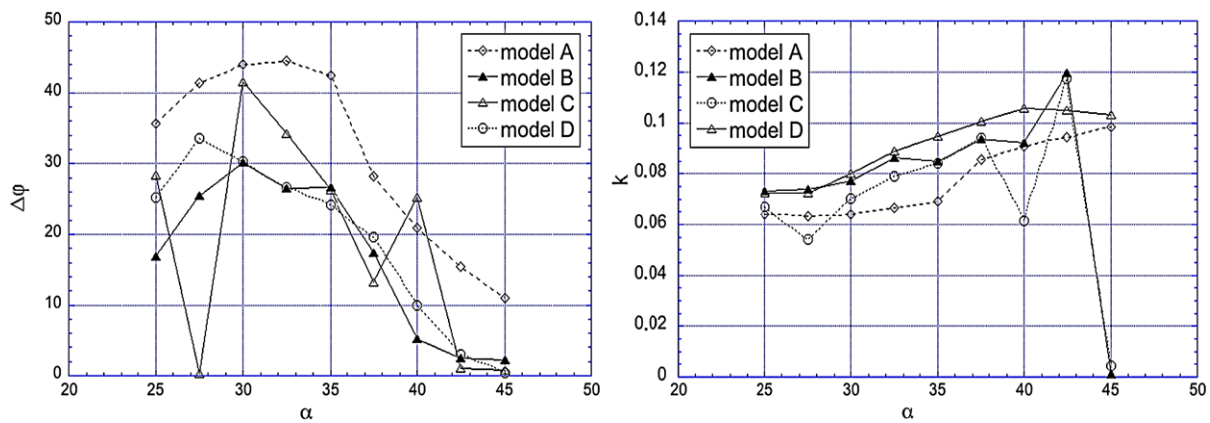

Fig. 5 Experimental data: effect of model configuration on amplitude and reduced frequency (models A, B, C, and D—$V = 30$ m/s, Re ≈ 950000)

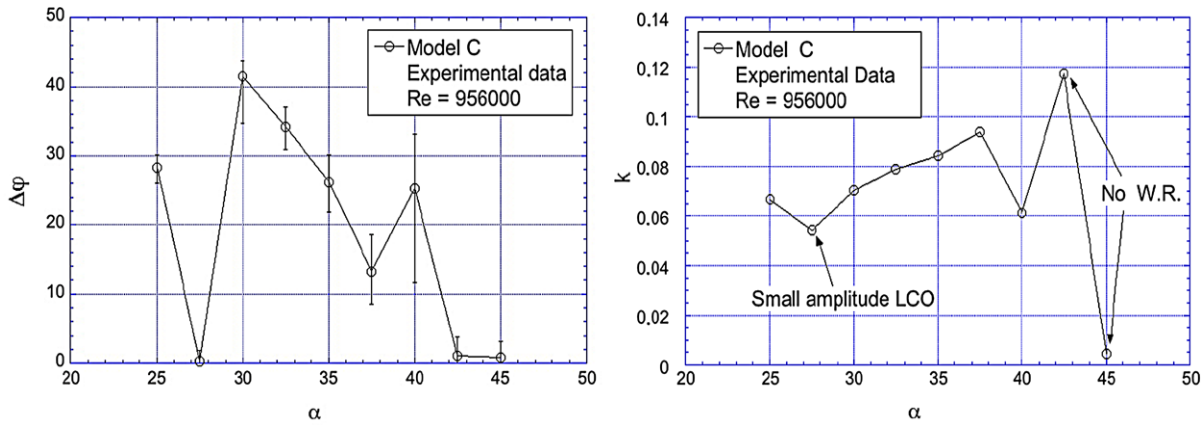

Fig. 6 Experimental data: amplitude and reduced frequency (model C—$V = 30$ m/s, Re ≈ 950000)

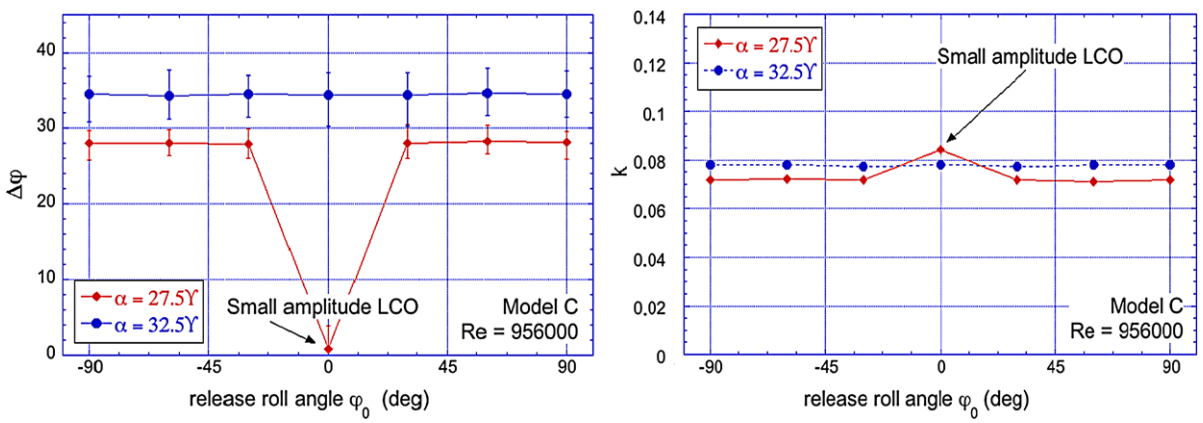

Fig. 7 Experimental data: effect of initial conditions on amplitude and reduced frequency (model C—$V = 30$ m/s, Re ≈ 950000)

the basic winged configuration (model A) that is less evident for the other models.

In Fig. 6, the limit cycle characteristics for model C are presented for $V = 30$ m/s and $\varphi_0 = 20°$. The limit cycle is stable for lower angles of attack only, and for $\alpha \geq 37.5°$ (wing vortex breakdown starts to occur) either the oscillation amplitude fluctuates or the motion disappears completely. As a matter of fact, the type of roll dynamics that is observed for the complete configuration is only partially described as a stable elliptical limit cycle. The reduced frequency does not exhibit a specific trend as a response to wing vortex breakdown (differently from model A) with a very large scatter for higher α.

The effect of initial conditions on the limit cycle characteristics for model C ($\alpha = 27.5°$ and $\alpha = 32.5°$) is presented in Fig. 7. No wing vortex breakdown is observed for $\varphi_0 = 0°$. The limit cycle is unaffected by the initial release roll angle φ_0. A similar result was found for model A in [12, 13]. The unique singularity is for $\alpha = 27.5°$ as several tests confirmed that wing rock is not triggered for initial conditions $\varphi_0 \approx 0$ and $V = 30$–35 m/s. The steady state is a small amplitude wing vibration in roll and the spectral frequency is still very close to the one of the limit cycle found for larger initial conditions. An explanation based on the analysis of the analytical model is presented later. Roll divergence or spinning are not seen in experiments for models A and C, since above a certain angle of attack (or alternatively for larger roll angles), vortex breakdown appears on the wing and it contributes a damping moment that reduces the steady state amplitude. Therefore, limit cycles are seen instead of divergence. The observation of roll divergence in wind tunnel experiments is also strongly affected by effective and virtual dihedral (i.e., the angular measure of lateral sta-

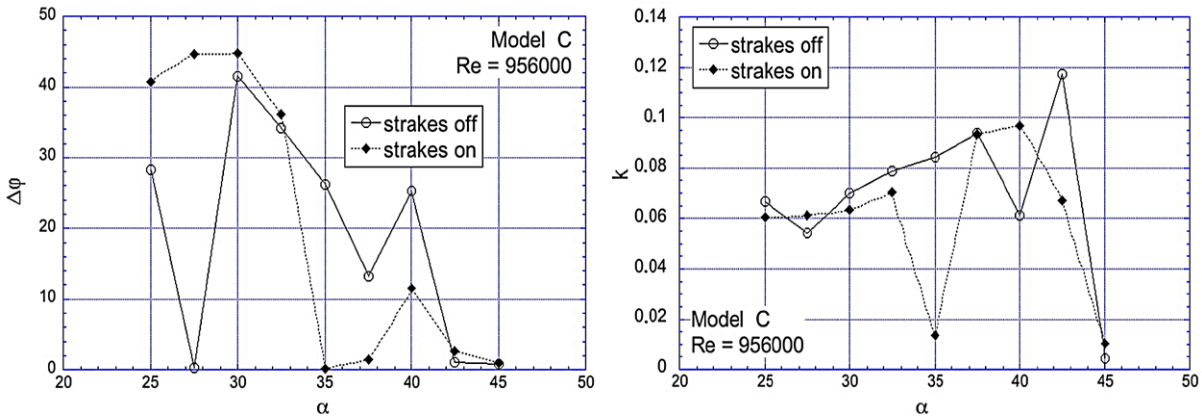

Fig. 8 Experimental data: effect of forebody strakes on amplitude and reduced frequency (model C—$V = 30$ m/s, Re ≈ 950000)

bility) for the model tested. Virtual dihedral is mainly changed by leading edge bevel angle, sting and model shapes. Another contributing element is the position of the axis of rotation that should be coincident with the inertial axis.

Static surface flow visualizations on model C (mini-tufts were glued on the upper part of the wing) show that, for $\alpha > 35°$, the wing vortices are led to asymmetry by the interference with forebody wake and vortical patterns.

The effect of forebody strakes on model C oscillatory response is presented in Fig. 8. The position and the size of the strakes was selected according to an empirical review of existing solutions [3]. These non-lifting devices force the forebody vortices to become symmetric neutralizing their natural tendency to asymmetry. They also affect the interference with the lifting surface. The oscillation amplitude $\Delta\varphi$ exhibits a behavior that is very similar to model A for $\alpha \leq 35°$. The wing rock oscillation disappears completely for $\alpha > 35°$ due to the anticipation of vortex breakdown induced by the interaction of forebody strakes with the flow emanating from the wing leading edge. The singularity for $\alpha = 27.5°$ is completely canceled and a stable limit cycle is reached even for $\varphi_0 \approx 0$. The reduced frequency is marginally affected. As expected, the strakes deflect and enforce the symmetric alignment of forebody vortices. These effects are tuned selecting their dihedral angle and their position along the forebody.

The parameters a_i (Fig. 9) were identified for models A and C by means of least-squares approximation of the experimental results with coherent test conditions. It can be said that, for $\alpha \leq 35°$, the coefficients a_0 and a_3 representing the restoring action (stiffness) are similar for both configurations while the coefficients a_1, a_2, and a_4 representing the damping action differ substantially. As a matter of fact, the presence of the fuselage alters the hysteresis mechanism, i.e., the damping of the system. For $\alpha > 35°$, no further consideration can be derived for the trend of the coefficients of models A and C. The only remark is that the coefficients for model A (see Fig. 10) still reproduce the oscillatory response (amplitude $\Delta\varphi$ and reduced frequency k) with accuracy in the complete α-range while the simulated response for model C fails to comply with experiments for $\alpha > 35°$ (see Fig. 11). The coefficients of the analytical model are obtained from numerical fit of experimental data derived with initial conditions internal to the final state, i.e., the extension of its validity to larger roll angles $60° < \Delta\varphi < 90°$ is not straightforward. As a matter of fact, the dynamic stability of trajectories with large angular perturbations should be investigated through other experimental methods (large amplitude direct forced oscillation techniques as an example [15]).

The steady state offset of limit cycle, measured from experiments and reproduced by the analytical model, is presented in Fig. 12. The experimental data for model A show a moderate constant offset due to support interference (not shown by the analytical model that is unable to reproduce asymmetric oscillatory cycles). The data for model C demonstrate that the complete configuration oscillates with an angular offset increasing up to $\Delta\varphi = 20°$ (an effect of asymmetry of forebody vortices). As expected, the analyt-

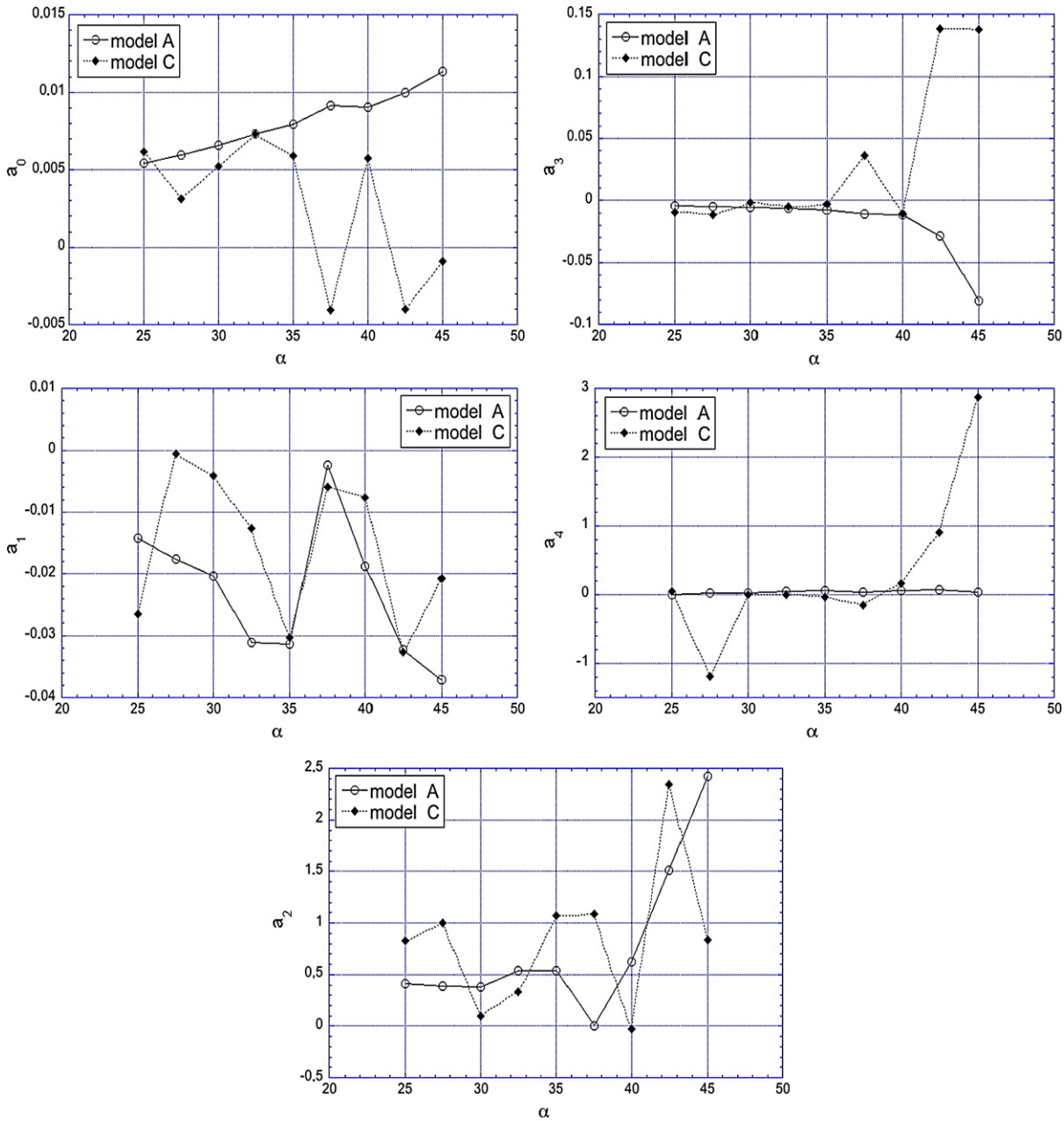

Fig. 9 Analytical model: fitting of experimental data (models A and C—$V = 30$ m/s, Re ≈ 950000)

ical model filters the presence of the offset with a unique exception for $\alpha = 42.5°$ (see Fig. 16) that is a nonoscillatory condition, i.e., the solution is attracted by the restoring actions providing a stable asymmetric trim.

A detailed analysis of the terms of the analytical model is given in Fig. 13 for model A at $\alpha = 30°$. The damping coefficient $(a_1 + a_4\varphi^2)$ is nonlinear and negative for $\varphi < \sqrt{-a_1/a_4}$ (Fig. 13). The system is dynamically unstable for lower roll angles becoming stable as φ increases up to the inversion point. The condition for equilibrium (limit cycle) is obtained as the balance between dissipation and generation of energy. Dynamic stability and limit cycle characteristics are also influ-

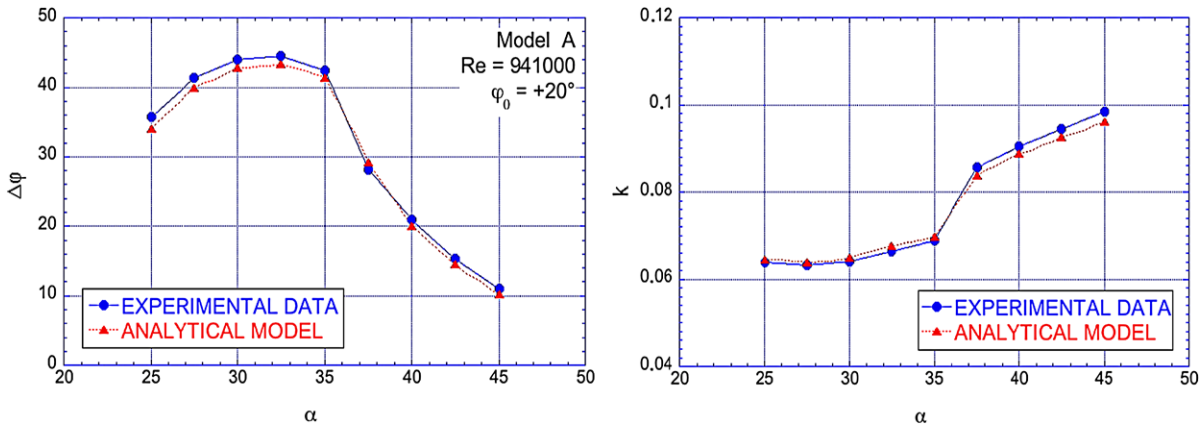

Fig. 10 Comparison of experimental data and model fitting: amplitude and reduced frequency (model A—$V = 30$ m/s, Re ≈ 950000)

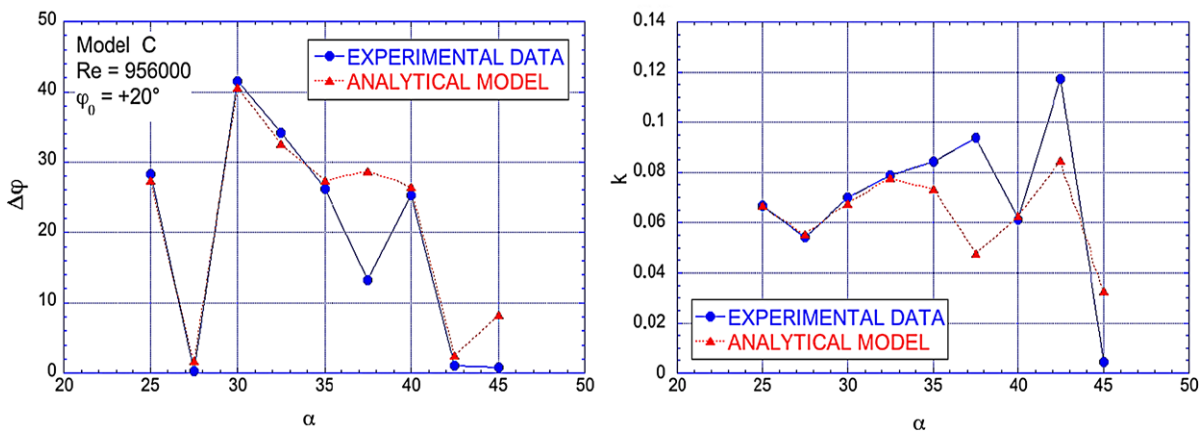

Fig. 11 Comparison of experimental data and model fitting: amplitude and reduced frequency (model C—$V = 30$ m/s, Re ≈ 950000)

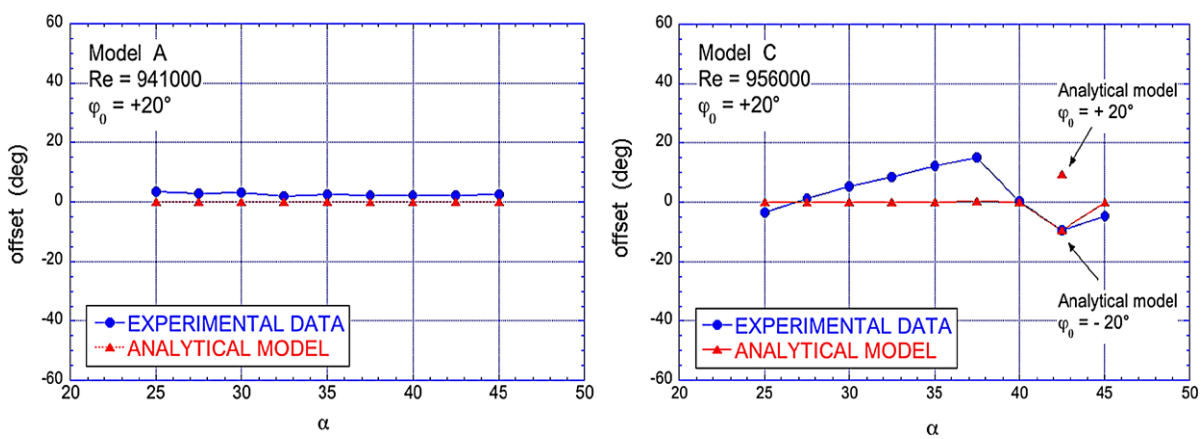

Fig. 12 Comparison of experimental data and model fitting: steady state offset (models A and C—V= 30 m/s, Re ≈ 950000)

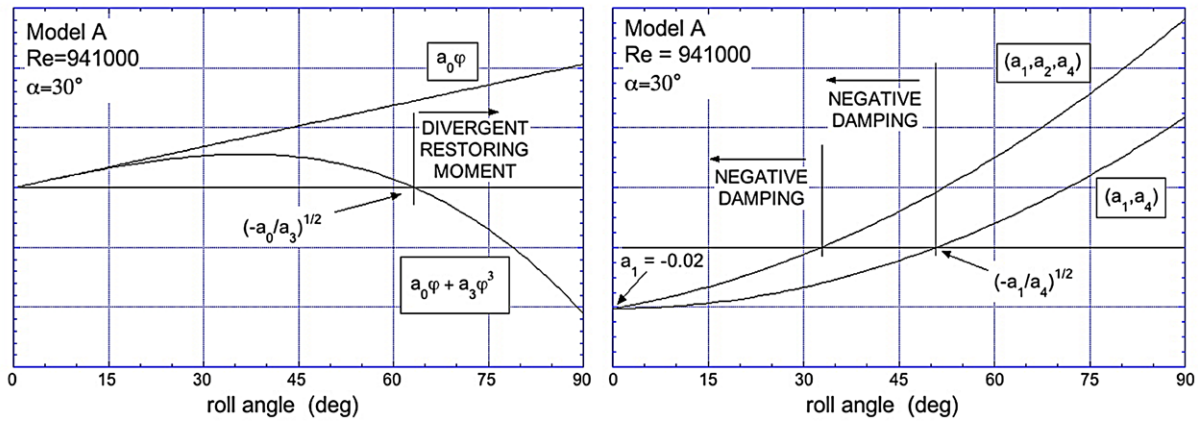

Fig. 13 Restoring and damping actions as modeled in the analytical model (model A—$\alpha = 30°$, $V = 30$ m/s, Re ≈ 950000)

enced by the additional damping produced by the term $a_2|\dot{\varphi}|\dot{\varphi}$, that shifts the transition angle from unstable to stable damping. The reduced order model

$$\ddot{\varphi} + a_0\varphi + a_3\varphi^3 = 0 \tag{6}$$

describes an undamped system with nonlinear stiffness. The restoring moment $a_0\varphi + a_3\varphi^3$ exhibits a typical trend with softening of linear stiffness a_0. As a consequence, the system is statically divergent for $\varphi > \sqrt{-a_0/a_3}$ (unstable trim point).

Model C shows an interesting singularity for $\alpha = 27.5°$ as wing rock oscillations are not triggered (see Fig. 14). After the release of the brake, model C converges to a nonoscillatory steady state without a build up phase. The one distinctive feature of model C with respect to models A, B, and D, is that only model C has both nose and forebody. Since none of the other models exhibit anything resembling the peculiar behavior of model C, it would seem that the characteristic behavior of this model would be strongly related with the distinctive features it contains. Therefore, it would seem that the interaction between the nose and forebody shed vortices, either exclusively or in combination with shed wing vorticity, can explain this unusual behavior. It is the interference between nose, forebody, and wing vortices that cancels out the hysteresis for the wing vortex normal displacements, the primary source of dynamic instability of the system (this singular behavior for $\alpha = 27.5°$ is canceled by the adoption of forebody strakes that alter the interference between forebody and wing vortices, delayed to higher angles of attack). The analysis of the equivalent analytical model explains the situation. The restoring torque is positive for lower roll angles $\Delta\varphi \leq 30°$ as expected, but the damping coefficient is always unstable (differently from the situation presented in Fig. 13 for model A). The level of negative unstable damping for $\varphi \approx 0$ and $\dot{\varphi} \approx 0$ is not sufficient to trigger the build up phase as the restoring effect is prevalent. This is confirmed by the experiments that did not exhibit wing rock oscillations for $-15° < \varphi_0 < 15°$ only. Larger initial conditions lead to large-amplitude limit cycle oscillations (see Fig. 14). The analytical model predicts oscillatory convergence for $|\varphi_0| < 8°$ while fails to match the experimental data for $|\varphi_0| > 8°$ (parametric refit based on experimental data obtained for $|\varphi_0| > 20°$ is required). Numerical experiments with the analytical model show that for $\varphi \approx 0$ minimal increments of the initial roll rate (prospin increments $\Delta\dot{\varphi} > 0.01$ rad/s) lead to divergence from symmetric flight. Here, it appears that there are more stable limit cycles than one: Different initial conditions can lead to at least two different motions, one small-amplitude and one large-amplitude limit cycle. If there are two stable limit cycles, then there is an unstable limit cycle between them (as found by the divergent response of the analytical model for increasing initial rate about $\varphi \approx 0$). Therefore, the basin of attraction for the small amplitude limit cycle is very narrow. Note that the parameters identified for $|\varphi_0| < 20°$ are unable to predict the large-amplitude attractor. The presence of some type of switching in the aerodynamics of the wing may explain the need for a scheduling of the parameters of the analytical model (critical state as suggested by [4]).

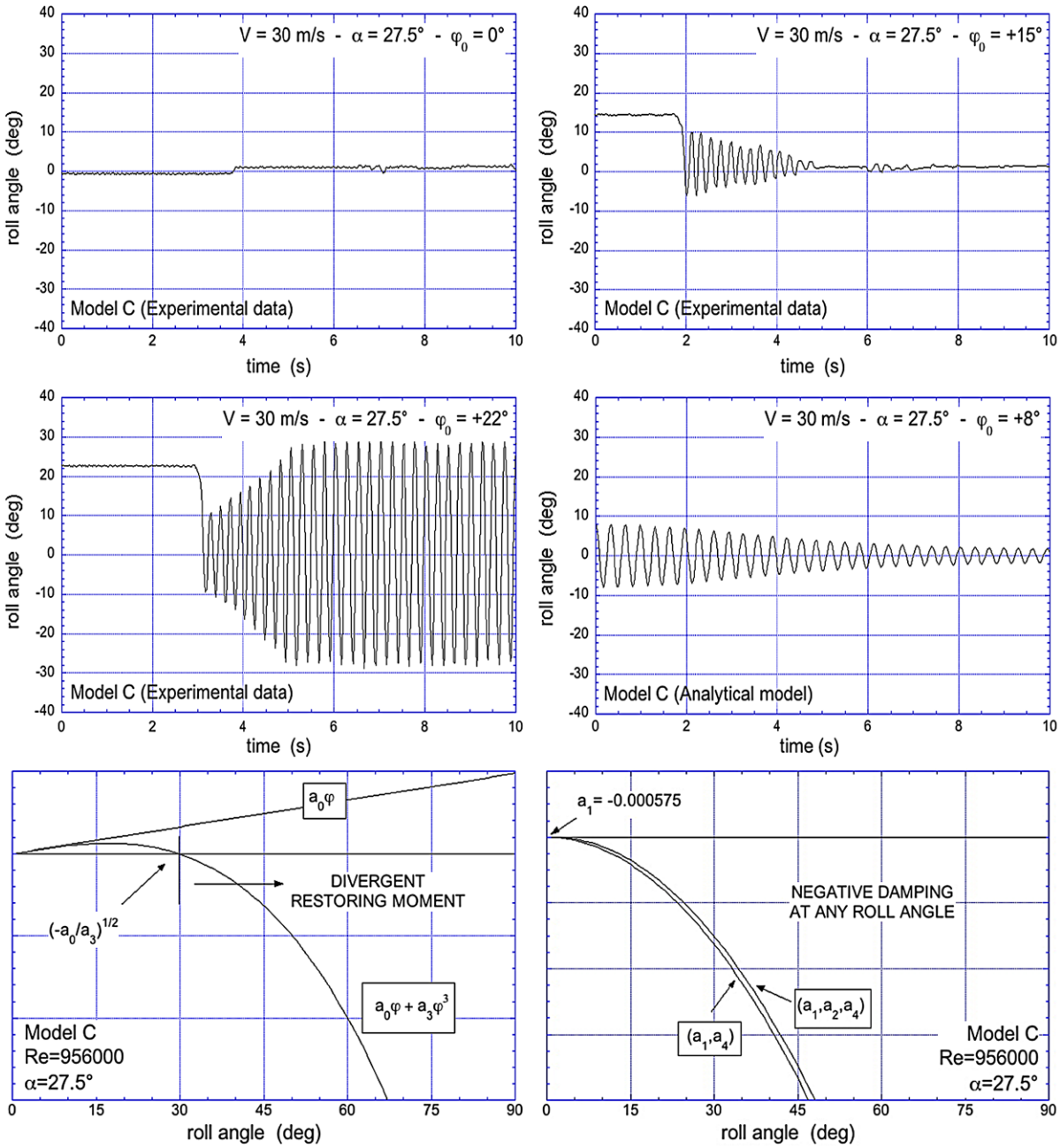

Fig. 14 Comparison of experimental data and analytical model response (model C—$\alpha = 27.5°$, $V = 30$ m/s, Re ≈ 950000)

A mismatch between experiments and analytical model for the configuration C at $\alpha = 37.5°$ is presented in Fig. 15. The experimental data demonstrate that, due to forebody vortex asymmetry, the axis of the limit cycle is shifted out bound at $\varphi \approx +19°$. The damping of the system, as identified by the analytical model, is unstable for the complete φ-range. The level of instability for $\varphi \approx 0$ is sufficient to trigger the build up phase and the motion is attracted by a statically stable trim point far from the condition of symmetry for the wing (unbalanced roll angle $\varphi \approx +19°$). The cubic form of the restoring moment $a_0\varphi + a_3\varphi^3$

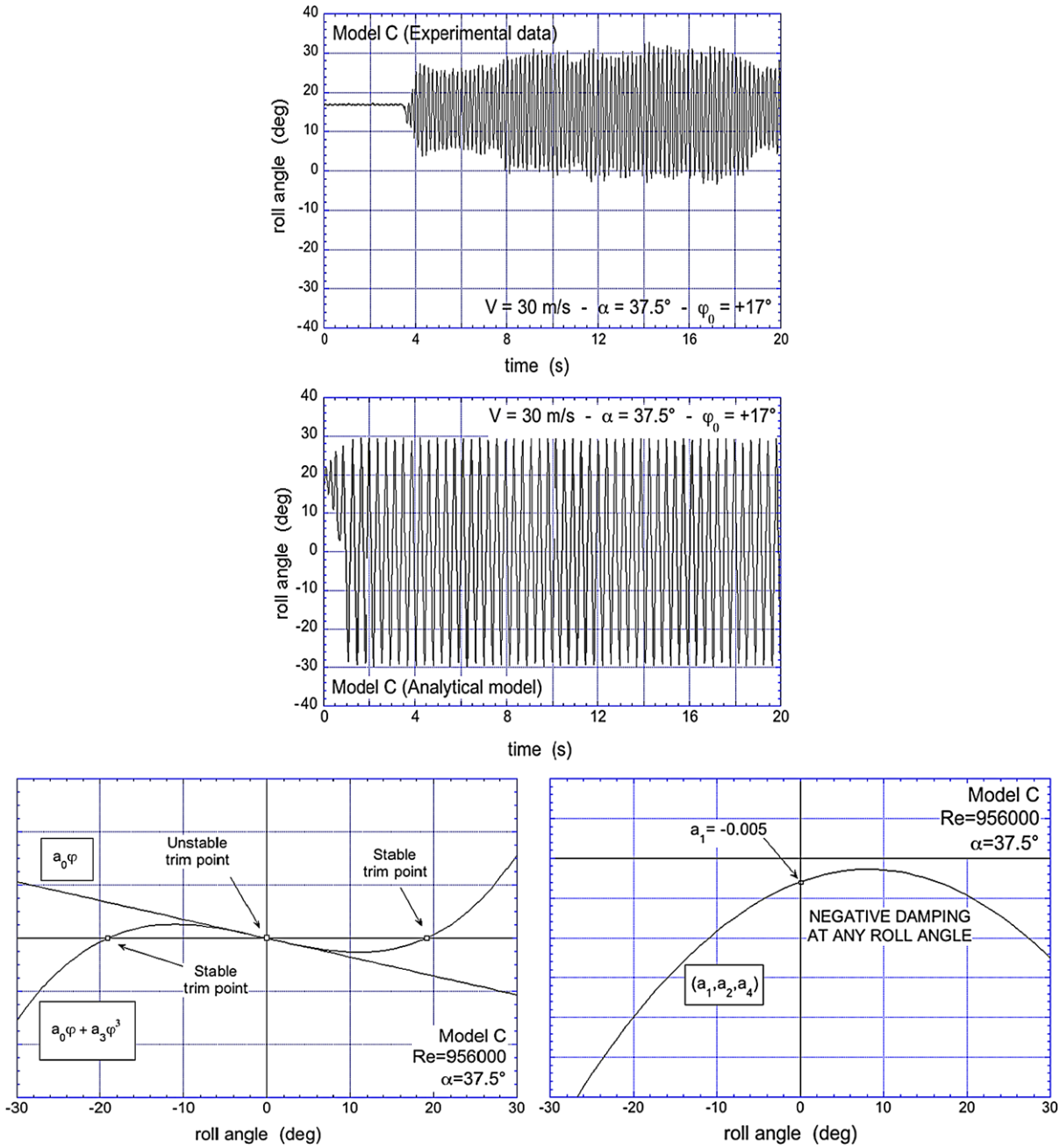

Fig. 15 Comparison of experimental data and analytical model response (model C—$\alpha = 37.5°$, $V = 30$ m/s, Re ≈ 950000)

introduces into the model a second artificial trim point for $\varphi \approx -19°$ (statically stable), enforcing a symmetric behavior not present in the real case. Therefore, the two attractors design the trajectory of the limit cycle described by the analytical model in a symmetric way. The dynamic instability drives the transition of the oscillation from one trim point to another. This discrepancy can only be corrected by adapting the form of the restoring torque to the effect of oscillation offsets.

The same situation is observed for model C at $\alpha = 42.5°$ as shown in Fig. 16. For this angle of attack, the wing rock is not triggered and the limit cycle

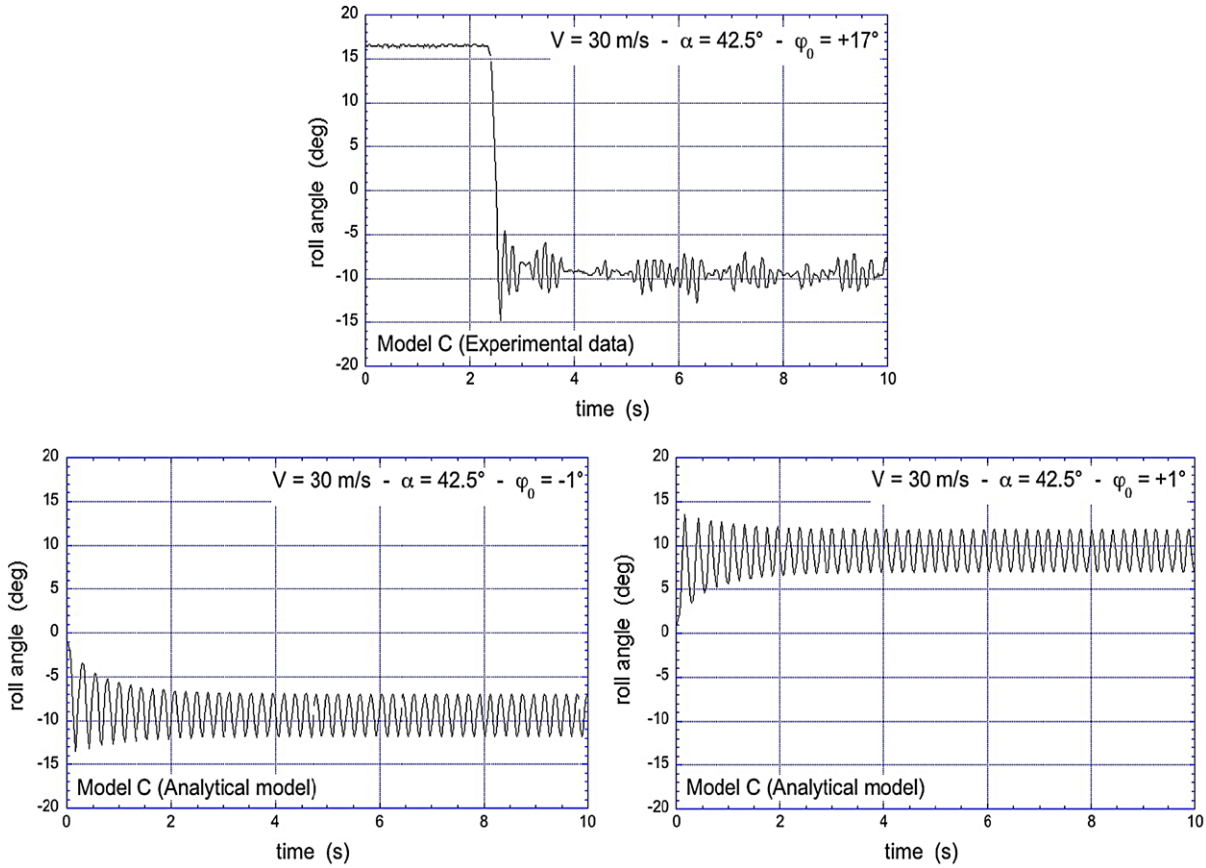

Fig. 16 Comparison of experimental data and analytical model response (model C—$\alpha = 42.5°$, $V = 30$ m/s, Re ≈ 950000)

is not recognized during the experiments. Simulating the response of the system with the analytical model provides convergence either to positive or negative roll offset, according to the sign of initial conditions. The levels of dynamic instability are not sufficient to drive the switch between the two trim points (stabilizing effect induced by wing vortex breakdown). Once again, the analytical model present a situation of symmetry that is artificial.

It must be underlined that when the analytical model fails to reproduce the wing rock response for model C at $\alpha = 37.5°, 42.5°$, and $45°$ the restoring torque is characterized by the presence of two separate symmetric stable trim points for $\varphi \neq 0$. On the contrary, when for lower α, the stable trim point is at $\varphi = 0$, the analytical model correctly reproduces the amplitude and the reduced frequency of the limit cycle, but it cannot model any offset of the cyclic trajectory. As a conclusion, the function $a_0\varphi + a_3\varphi^3$ cannot fit or model asymmetric flight states as those induced by forebody vortex asymmetries.

Starting from the analytical model, the sign of stiffness and damping aerodynamic terms is obtained (see Fig. 17). Model A exhibits a uniform separation of roll angle ranges for dynamic stability that is the driving mechanism of wing rock dynamics. Note that the amplitude of the limit cycle falls in the intermediate range of the separation lines (i.e., where static convergence and dynamic stability coexist). A wide area of static divergence is predicted for large roll angles. As previously discussed, divergence was never observed during the experiments. The analytical model actually fails to represent the restoring torque contribution for larger roll displacements. Model C shows a more complicated pattern with a less uniform distribution of the relevant areas. Static divergence is still found for very large roll angles. The statically stable trim points with offset found for higher angles of attack are marked on the diagram. The range for dynamic stability is quite

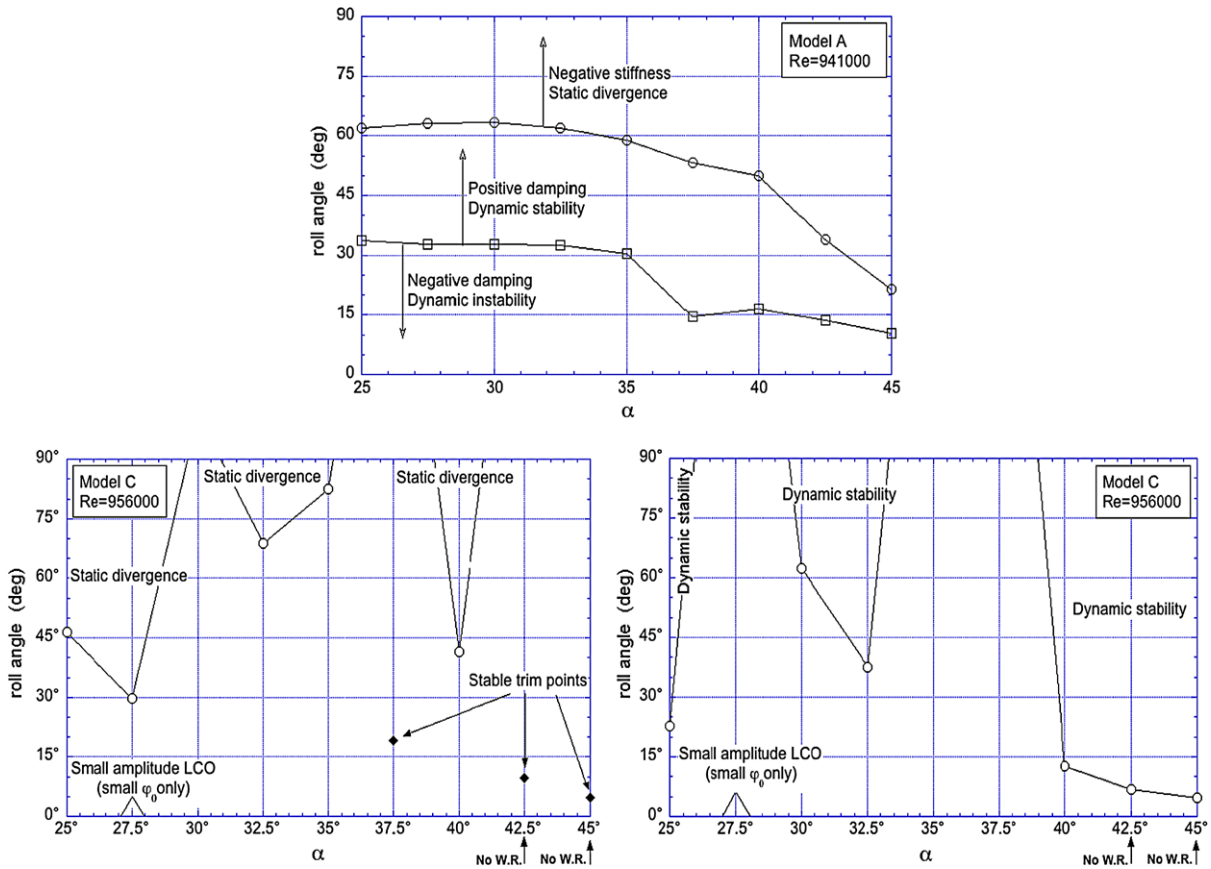

Fig. 17 Analysis of stiffness and damping aerodynamic torques

extended for higher attitudes shrinking the amplitude of the oscillatory limit cycle for $\alpha > 40°$. The model overestimates the extension of the dynamically unstable region for $\alpha \approx 27.5°$. This explains the inability of the model to reproduce the large-amplitude limit cycle oscillation observed during the experiments. Finally, the area compatible with the small-amplitude limit cycle is defined in compliance with the numerical simulations performed with the analytical model.

5 Concluding remarks

A complete set of free-to-roll wind tunnel experiments has been performed on a 80° delta wing, with and without a modular fuselage kit. A special set of experiments has been devoted to the understanding of the effect of airspeed and initial conditions on limit cycle characteristics of model C (complete model with slender forebody).

The results for the basic model (model A) confirm the previous set of data presented in [12, 13].

The experiments on the complete model with slender forebody (model C) outline a relevant effect of angle of attack on limit cycle characteristics, as for some model attitudes wing rock is not triggered or even suppressed. The explanation is a more complicated flow pattern, including the forebody vortices as a driving mechanism of interference with the wing vortices and promoting vortical asymmetries for symmetric flight, never observed for the basic winged model (model A).

The effect of airspeed (Reynolds number) is marginal and limit cycle parameters (amplitude and reduced frequency) are unchanged as airspeed is varied within the limits used for the present testing activity. A singular behavior was observed for model C at $\alpha = 27.5°$ and $V = 30$–35 m/s, where wing rock oscillations are unexpectedly not triggered.

The initial release roll angle does not affect the limit cycle of model A (the limit cycle is a stable

unique attractor), changing the build up transient phase only. Differently, the complete model (model C) exhibits an occasional sensitivity to the initial conditions φ_0, precluding the build up of the oscillations. When the motion is triggered, the limit cycle characteristics still remain unaffected.

The comparison of experimental data shows that the presence of the fuselage alters the damping term as observed by the decrease of final state amplitudes and the increase of oscillation frequency.

Static surface flow visualizations on model C (mini-tufts were glued on the upper part of the wing) show that, for $\alpha > 35°$, the wing vortices are led to asymmetry by the interference with forebody wake and vortical patterns.

The analytical model derived and successfully validated for model A in [12, 13] was here applied to the complete model case. The analytical model complies with the experimental oscillation time histories measured on model C for $\alpha \leq 35°$, while for higher angles of attack the presence of forebody vortices changes substantially the shape of the function describing the restoring moment (the softening formulation $a_0\varphi + a_3\varphi^3$ adopted in the differential equation describing wing rock roll dynamics). Attempts to correct the formulation did not produce a complete solution for this problem.

Acknowledgements The author wishes to acknowledge the invaluable technical assistance given by Mr. Andrea Bussolin.

References

1. Hsu, C.H., Lan, C.E.: Theory of wing rock. J. Aircr. **22**(10), 920–924 (1985)
2. Malcolm, G.N.: Forebody vortex control. Prog. Aerosp. Sci. **28**(3), 171–234 (1991)
3. Cooperative programme on dynamic wind tunnel experiments for manoevring aircraft. NATO AGARD Advisory Report 305 (1996)
4. Nelson, R.C., Pelletier, A.: The unsteady aerodynamics of slender wings and aircraft undergoing large amplitude maneuvers. Prog. Aerosp. Sci. **39**, 185–248 (2003)
5. Katz, J.: Wing-vortex interactions and wing rock. Prog. Aerosp. Sci. **35**, 727–750 (1999)
6. Levin, D., Katz, J.: Dynamic load measurements with delta wings undergoing self induced roll oscillations. J. Aircr. **21**(1), 30–36 (1984)
7. Nguyen, L.T., Yip, L.P., Chambers, J.R.: Self induced wing rock of slender delta wings. In: AIAA Atmospheric Flight Mechanics Conference, Albuquerque, NM (1981)
8. Arena, A.S. Jr.: An experimental and computational investigation of slender wings undergoing wing rock. Ph.D. Dissertation, University of Notre Dame, IN (1992)
9. Arena, A.S. Jr., Nelson, R.C.: An experimental study of the nonlinear dynamic phenomenon known as wing rock. AIAA Paper 90-2812 (1990)
10. Arena, A.S. Jr., Nelson, R.C.: Measurement of unsteady surface pressure on a slender wing undergoing a self induced oscillation. Exp. Fluids **16**(6), 414–416 (1994)
11. Yoshinaga, T., Tate, A., Noda, J.: Wing rock of delta wings with an analysis by the phase plane method. In: AIAA Atmospheric Flight Mechanics Conference, Monterey, CA (1993)
12. Guglieri, G., Quagliotti, F.B.: Experimental observation and discussion of the wing rock phenomenon. Aerosp. Sci. Technol. **1**(2), 111–123 (1997)
13. Guglieri, G., Quagliotti, F.B.: Analytical and experimental analysis of wing rock. Nonlinear Dyn. **24**(2), 129–146 (2001)
14. Nayfeh, A.H., Elzebda, J.M., Mook, D.T.: Analytical study of the subsonic wing rock phenomenon for slender delta wings. J. Aircr. **26**(9), 805–809 (1989)
15. Hanff, E.S.: Large amplitude oscillations. AGARD-R-776 (1991)
16. Konstadinopoulos, P., Mook, D.T., Nayfeh, A.H.: Subsonic wing rock of slender delta wings. J. Aircr. **22**(3), 223–228 (1985)
17. Quast, T., Nelson, R.C., Fisher, D.F.: A study of high alpha dynamics and flow visualization for a 2.5 % model of the F-18 HARV undergoing wing rock. In: AIAA Applied Aerodynamics Conference, Baltimore, MD (1991)
18. Quast, T.: A study of high alpha dynamics and flow visualization for a 2.5 % model of the F-18 HARV undergoing wing rock. M.S. Thesis, University of Notre Dame, IN (1991)